Hindawi
Advances in Materials Science and Engineering
Volume 2019, Article ID 4270310, 15 pages
https://doi.org/10.1155/2019/4270310

Research Article

Synthesis and Application of Fe-Doped TiO_2-Halloysite Nanotubes Composite and Their Potential Application in Water Treatment

Emmanuel Nyankson, Benjamin Agyei-Tuffour, Jonas Adjasoo, Annan Ebenezer, David Dodoo-Arhin, Abu Yaya, Bismark Mensah, and Johnson Kwame Efavi

Materials Science and Engineering Department, University of Ghana, P.O. Box LG 77, Legon-Accra, Ghana

Correspondence should be addressed to Johnson Kwame Efavi; jkefavi@ug.edu.gh

Received 27 September 2019; Accepted 16 November 2019; Published 12 December 2019

Academic Editor: Stefano Bellucci

In this work, the potential application of TiO_2-Fe-HNT photocatalyst-adsorbent composite in water treatment technologies was confirmed. The photocatalyst-adsorbent composite (TiO_2-Fe-HNTs) was synthesized by the hydrothermal method and characterized by X-ray diffraction, thermogravimetric analysis, Fourier-transform infrared spectroscopy, scanning electron microscopy-energy dispersive X-ray spectroscopy, and diffuse reflectance spectroscopy. The adsorption and photocatalysis mechanism by the TiO_2-Fe-HNT composite were examined on methylene blue dye, rhodamine blue dye, naproxen sodium (pharmaceutical drug waste), and imidacloprid (pesticide). The TiO_2-Fe-HNT composite was active in UV and visible regions of the electromagnetic spectrum. The adsorption and photocatalytic efficiency increased with increasing amount of HNTs. The photocatalyst-adsorbent composite exhibited excellent removal efficiency for pharmaceutical waste (naproxen sodium) and pesticides (imidacloprid). An adsorption equilibrium data fitted well with the pseudo-second-order kinetics for both methylene blue and rhodamine blue dyes with the intraparticle model describing its rate-controlling steps. The Langmuir and Freundlich isotherm models further described the adsorption of methylene blue and rhodamine blue molecules, respectively.

1. Introduction

One of the major problems faced by humanity all over the world is poor water quality. Over 2 billion people globally do not have access to potable water. 8% of this number collects drinking water directly from surface water sources such as lakes and rivers [1]. The increase in human population with its associated increase in industrialization and climate change is expected to result in an increase in demand for safe water [2]. The number of people not having access to safe water is expected to grow due to increased water contamination from industrial and human activities. The major pollutants found in surface and ground water bodies include water-soluble dyes [3], pharmaceutical waste [4], agrochemicals [5], heavy metals [6], microorganisms [7], and hydrocarbons [8]. The presence of these pollutants may have a detrimental effect on aquatic species and humans that utilize the contaminated water in their daily activities. Contaminated water is associated with the transmission of diseases such as hepatitis A, cholera, diarrhea, and dysentery. The WHO organization has reported that approximately 845000 people die from diarrhea each year [9]. Water pollution has associated economic and social impact such as increase in expenditure on health, long risky journeys to collect portable water, and poor school attendance due to ill health. To render water bodies safe for use, these pollutants must be removed, and therefore, different water treatment technologies have been developed to reduce the worsening of clean water shortage and also meet the increased demand for potable water [10].

The different water treatment technologies can be categorized into three: tertiary, secondary, and primary [11]. The primary treatment technology includes physical and chemical purification processes such as filtration, sedimentation, and coagulation, while the secondary treatment technology includes biological purification processes such as

aerobic and anaerobic processes. On the contrary, oxidation and advanced oxidation processes, adsorption, distillation, and solvent extraction can be categorized under tertiary treatment technologies [3, 11]. The right method to be adopted during water treatment is dependent on the extent of pollution and the nature of the pollutant.

Water bodies polluted by dyes, pharmaceutical waste, and pesticides can be treated through advanced oxidation processes (AOPs). In AOPs, reactive oxygen species (e.g., hydroxyl radicals), which aid the degradation of pollutants which are resistant to conventional treatment methods are produced. The pollutants are degraded into innocuous compounds such as H_2O, CO_2, and mineral acids [12]. AOPs which include sonolysis, Fenton processes, photocatalysis, and the use of UV radiation and hydrogen peroxide are nontoxic and economical and can degrade different types of organic pollutants [3]. Photocatalysis is one of the most widely studied AOPs, and its potential in the degradation of dyes has been examined on different photocatalysts such as TiO_2 [13], Ag_3PO_4 [14], TiO_2-Ag [15], and ZnO [16]. Photocatalysis involves (a) the absorption of photons (the energy of the photons must be greater than the bang gap energy), (b) excitation of photogenerated electrons from the valence band (VB) to the conduction band (CB) generating electron-hole pair, and (c) oxidation of adsorbed pollutants by the VB hole which is strongly oxidizing. The CB electrons which are strongly reducing can be used to create reactive oxygen species that can attack pollutants and degrade them [13]. TiO_2 is a semiconductor photocatalyst and has been investigated by many researchers. TiO_2 photocatalyst is stable, relatively cheaper, nontoxic, and readily available [17]. However, the large band gap of TiO_2 (~3.0–3.2 eV) has restricted its photoactivity to the UV region of the electromagnetic spectrum [18]. TiO_2 can be made active in the UV-Vis region of the solar spectrum by doping and by coating the surface of TiO_2 [15] with a metal. Among the transition metal ions, Fe^{3+}-doped TiO_2 has resulted in an enhanced photocatalytic activity. The ionic radius of Fe^{3+} is almost the same as that of Ti^{4+}; hence, Fe^{3+} can be easily integrated into the structure of TiO_2 [19]. The reduction of the electron-hole recombination after doping with Fe is responsible for the enhanced photocatalytic activity of Fe-doped TiO_2 [20].

The synergistic effect of adsorption and photocatalysis has been investigated by researchers. The synergistic effect that resulted from the adsorption properties of activated carbon (AC) powders and photocatalytic properties of TiO_2 has been reported. The AC-TiO_2 composite recorded an enhanced photocatalytic and pollutant removal efficiency when compared with that of pristine TiO_2 [3, 21]. The synergistic relationship between adsorption and photocatalysis has been further examined by Sun et al. using the TiO_2-sulfanyl-AC composite [22]. The enhanced pollutant removal efficiency by these composites can be linked to the excellent adsorption capacity of AC. The incorporation of adsorbent into photocatalyst therefore offers a new design for developing photocatalyst-adsorbent system with enhanced pollutant removal/degradation efficiency. In addition to AC, other adsorbent materials such as zeolite [23], graphene [24], SiO_2 [25], Al_2O_3 [26], and multiwalled carbon nanotubes [27] have been used to develop photocatalyst-adsorbent systems. The adsorbent materials used in developing these composite adsorbent-photocatalyst systems have been reported to be expensive. In addition, there are problems associated with their treatment and regeneration [28]. More so, application of TiO_2 limits the practical usage to the UV region of the solar spectrum [29].

Halloysite nanotubes (HNTs) are natural 1 : 1 aluminosilicate material made up of an octahedron alumina sheet and tetrahedron silica sheet. HNTs possess rolled hollow nanotubular structure with high specific surface area of ca. 65 m^2/g. The diameter and length of HNTs vary from ~15 to 100 nm and 500 to 1100 nm, respectively [30]. Halloysite nanotubes have high adsorption capacity and are biocompatible, relatively cheap, readily available, and nontoxic. These unique properties of HNTs have enabled them to be used in different applications such as oil spill remediation, drug delivery systems, electronics, catalysis, water purification, and composite materials for construction [31–35]. Unlike the different adsorbent materials used in developing adsorbent-photocatalyst systems, naturally occurring HNTs are readily available and are low cost when compared with carbon nanotubes.

The synergistic effect of photocatalysis and adsorption by the TiO_2-Fe-HNT composite has not been widely investigated. The TiO_2-Fe-HNT adsorbent-photocatalyst composite was developed by the hydrothermal method and characterized by XRD, TGA, FTIR, SEM-EDX, and DRS. The synergistic effect of adsorption and photocatalysis by the synthesized TiO_2-Fe-HNT composite was examined on methylene blue dye, rhodamine blue dye, naproxen sodium (pharmaceutical waste), and imidacloprid (pesticide). An adsorption equilibrium studies was carried out using the water-soluble dyes (methylene blue and rhodamine blue dyes) and fitted with the Freundlich and Langmuir adsorption equilibrium isotherms, respectively. In addition, adsorption kinetics data were obtained and fitted with pseudo-first and pseudo-second-order kinetics and the intraparticle diffusion model.

2. Materials and Methods

2.1. Materials. Halloysite nanoclay (HNTs), titanium (IV) isopropoxide (TTIP), isopropyl alcohol (IPA), nitric acid (HNO_3), Fe (III) chloride, methylene blue, rhodamine B, naproxen sodium, imidacloprid, benzoquinone, ethylenediamine tera-acetic acid sodium, and dimethyl sulfoxide (DMSO) were obtained from Sigma-Aldrich, UK.

2.2. Synthesis of TiO_2-Fe-HNTs. Three different solutions were prepared and labeled A, B, and C. Solution A was prepared by adding 3.8 mL of TTIP to 19 mL of IPA under constant stirring. Acid solution with a pH of ca. 1.5 was prepared using HNO_3 and labeled as Solution B. 2 mL of Solution B was added dropwise to Solution A while stirring followed by addition of a calculated amount of $FeCl_3$ (Solution C). The resulting solution C was continuously stirred

for 90 minutes. At the same time, a calculated amount of HNTs was added to 20 mL of IPA and sonicated for 90 minutes. The dispersed HNTs in IPA were added to Solution C and agitated continuously for another 90 minutes. The resulting solution was transferred into an autoclave (hydrothermal reactor) and heat treated at 180°C for 3 hours. The obtained TiO_2-Fe-HNT particles were centrifuged and washed repeatedly with DI water. The particles were dried under vacuum at 70°C overnight. The amount of $FeCl_3$ added was varied to prepare samples with 1 and 2 wt.% Fe. The amount of the HNTs added resulted in the formation of sample with 25, 50, and 60 wt.% HNTs. $FeCl_3$ and HNTs were not included during the synthesis of TiO_2.

2.3. Characterization. X-ray powder diffraction (XRD) analysis was conducted on the adsorbent-photocatalyst composite using the Bruker D8 diffractometer-fitted LynxEye detector. Cu-Kα radiation ($\lambda = 0.15405$ nm) and a 2theta angular range of 10–80° were used. Field Electron and Ion (FEI) Nova NanoSEM connected to the energy dispersive X-ray acquisition detector was used to study the morphology and elemental composition of the TiO_2-Fe-HNT composite. Fourier-transform infrared (FTIR) spectroscopy was carried out using a Bruker Tensor 2027 FT-IR instrument. TA Instrument Q500 was used to analyze the thermal behavior (TGA). The TGA was conducted under nitrogen gas at the heating rate of 10°C/min. The diffuse reflectance spectroscopy (DRS) was conducted using the Ocean Optics USB-4000 UV-Vis spectrometer. The synthesized nanocomposites were compressed into a flat film prior to measurement.

2.4. Photocatalysis Experiment. The photocatalysis was conducted using the tungsten halogen UV-Vis light source. The photocatalytic activity was conducted on methylene blue, rhodamine B, naproxen sodium, and imidacloprid. In the typical photodegradation procedure, 200 mL of methylene blue solution (10 mg/L) in deionized water was used with a photocatalyst suspension concentration of 0.5 g/L. The methylene blue-photocatalyst mixture was stirred in the dark for 30 minutes and then irradiated with the tungsten halogen UV-Vis light source. Detailed adsorption studies revealed that the adsorption of dye molecules on the composite material was complete in 30 minutes. 2 mL aliquots were taken at different time intervals and centrifuged (at 6000 rpm for 10 minutes). The dye absorbance was quantified using a UV-Vis spectrometer (at $\lambda = 665$ nm). A similar procedure was used for the photocatalytic degradation of rhodamine dye (10 mg/L), naproxen sodium (8 mg/L), and imidacloprid (8 mg/L). The absorbance was taken at ~554, ~230, and ~269 nm for rhodamine B, naproxen sodium, and imidacloprid, respectively.

2.5. Absorption Experiment. The absorption of methylene blue and rhodamine B from aqueous solution was conducted using a batch method. A calculated amount of TiO_2-Fe-HNTs was added to 200 mL of different concentrations of the dye solution (2, 4, 6, 8, and 10 mg/L) and stirred continuously. 2 mL of the dye solution was sampled at different time intervals and centrifuged (6000 rpm for 10 minutes) to remove the particles. The absorbance of the supernatant was taken at a wavelength of 665 nm and 554 nm for methylene blue dye and rhodamine B dye, respectively, using the UV-Vis spectrometer.

All the experiments in this paper were repeated in triplicates, and the standard mean errors were calculated (represented as error bars in the Figures 1–3). The error bars were calculated from different measurements of the same sample.

3. Results and Discussion

3.1. Structural, Thermal, and Functional Groups Characterization. The XRD patterns of TiO_2 and TiO_2-Fe-HNT composite are shown in Figure 4. The crystallographic planes (101), (004), (200), (105), (211), (204), and (215) are characteristics peaks of anatase TiO_2 (JCPDS No. 21-1272). It was observed that the crystallinity of TiO_2 decreased upon the addition of Fe and HNTs. This was deduced from the broadening of the peaks. An increase in the amount of the Fe decreased the crystallinity of the synthesized composite. This is because the Fe atoms acted as defects in TiO_2. This distorted the crystal structure of TiO_2 and hindered the crystallinity of TiO_2 [36]. The characteristic peak (110) of HNTs was observed.

The XRD confirmed the synthesis of the TiO_2-Fe-HNT composite. The characteristic peak of Fe was not observed probably due to the relatively lower concentration of Fe used in the synthesis of the composite.

Thermogravimetric analysis of the synthesized TiO_2, TiO_2-Fe-HNTs, and HNTs was performed, and the results are presented in Figure 5. All the plots depict a multistage decomposition with relatively stable intermediate products. TiO_2 recorded two significant weight losses. There was ca. 5.1 wt.% loss when TiO_2 was heated from 60 to 250°C and ca. 1 wt.% when heated from 250 to 400°C. The weight of TiO_2 remained constant at heat treatments above 400°C. The total weight loss after heat treatment was ca. 6.1%. On the contrary, HNTs recorded ca. 5.3 wt.% loss at temperatures between 60 and 400°C. Increasing the temperature from 400 to 540°C resulted in an additional 11.3 wt.% loss. A total of 16.6 wt.% loss was recorded for HNTs. The TGA curve for the composite TiO_2-Fe-HNTs was a combination of the curves of HNTs and TiO_2. The total weight loss recorded over the entire temperature at which the heat treatment was carried out was ca. 12.5%. The TGA curve of the composite confirmed the presence of TiO_2 and HNTs.

The FTIR spectrum of the prepared TiO_2-Fe-HNT composite showed three additional peaks that were not observed in the spectrum of TiO_2 (Figure 6), suggesting the presence of HNTs in the composite. The broad band below 1000 cm^{-1} was ascribed to the stretching vibration of Ti-O [37, 38]. The strong peak at 1623 cm^{-1} corresponds to the symmetric vibration of absorbed water [39]. The broad peak at 3373 cm^{-1} was attributed to the stretching vibrations of the O-H functional group. The presence of HNTs in the

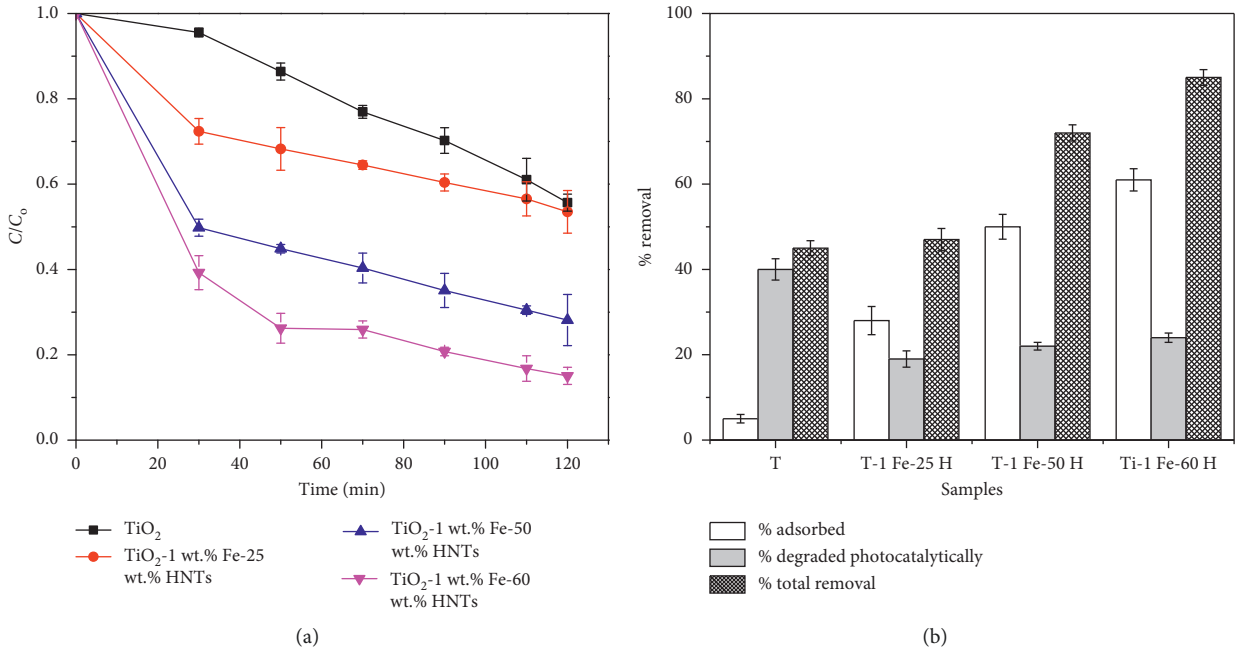

FIGURE 1: (a) Photocatalytic degradation and adsorption of methylene blue by TiO_2 and TiO_2-Fe-HNTs. (b) Summary of the performance of the synthesized TiO_2 and TiO_2-Fe-HNTs (T: TiO_2; T-Fe-H: TiO_2-Fe-HNT composite).

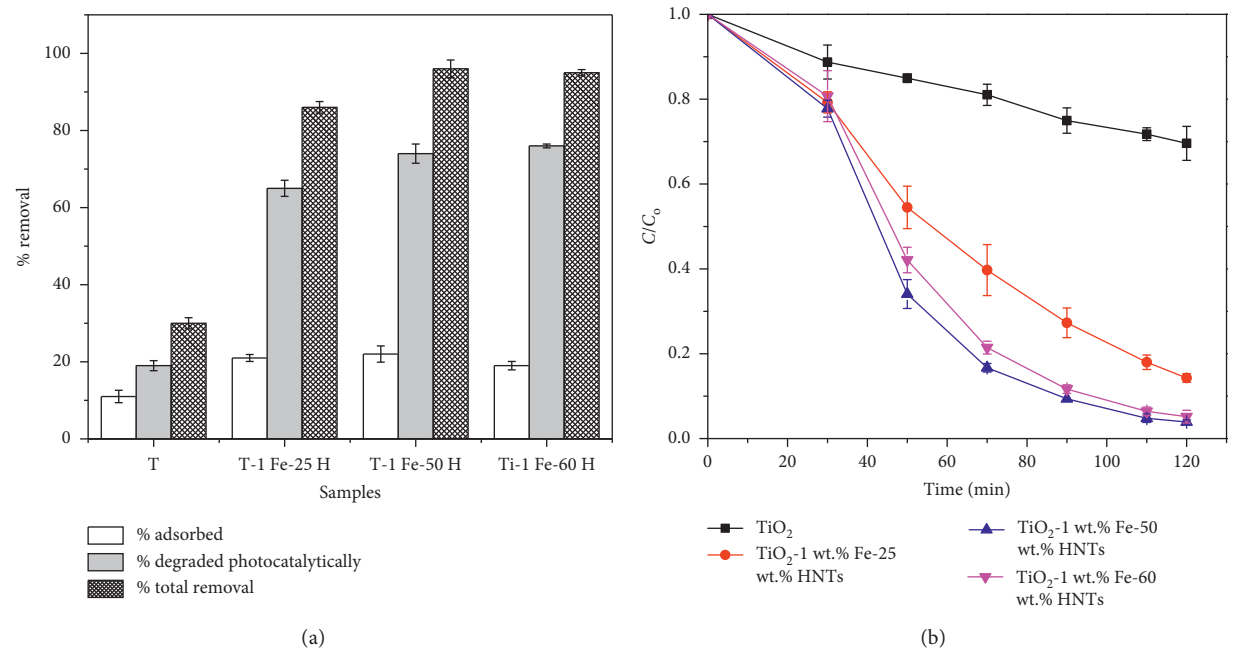

FIGURE 2: (a) Photocatalytic degradation and adsorption of rhodamine blue by TiO_2 and TiO_2-Fe-HNTs. (b) Summary of the performance of the synthesized TiO_2 and TiO_2-Fe-HNTs (T: TiO_2; T-Fe-H: TiO_2-Fe-HNT composite).

composite material resulted in the appearance of three other peaks at 912, 1118, and 1032 cm^{-1}. The band at 912 cm^{-1} resulted from the deformation vibration of the inner O-H groups present in HNTs. Stretching vibration of Si-O-Si was observed at 1032 cm^{-1}, whereas apical Si-O stretching mode resulted in a peak at 1118 cm^{-1} [32].

3.2. Structural Morphology, Elemental, and Optical Characterization. The structural morphology and elemental characterization of the composite was investigated through SEM-EDX analysis. The SEM images and the energy dispersive X-ray spectroscopy analysis are presented in Figure 7.

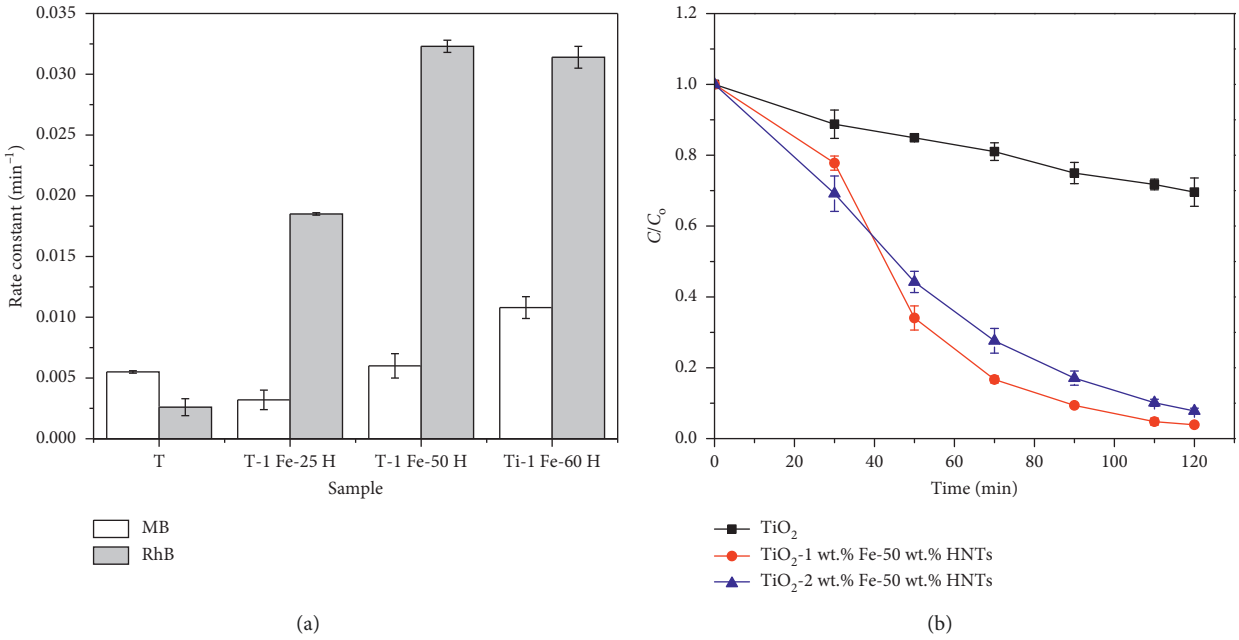

Figure 3: (a) Pseudo-first-order rate constants for photodegradation of rhodamine B (RhB) and methylene blue (MB). (b) Effect of Fe wt.% on the photodegradation efficiency of TiO_2-Fe-HNT composite (rhodamine B).

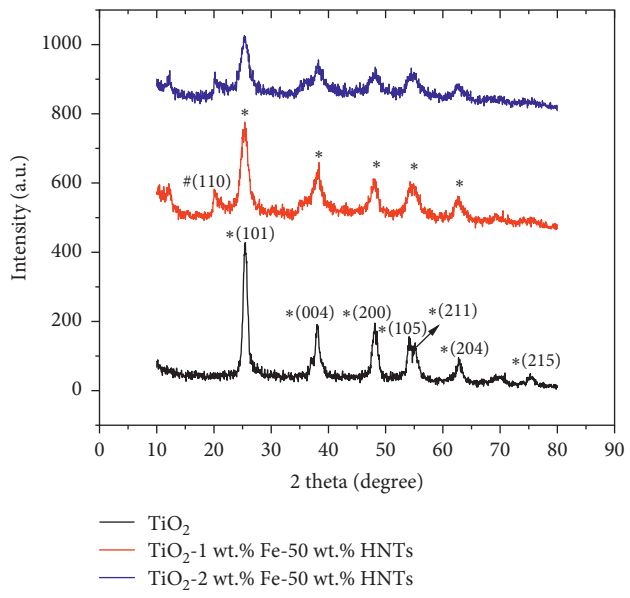

Figure 4: X-ray diffraction pattern of TiO_2 and TiO_2-Fe-HNTs ("∗" and "#" represents the crystallographic planes of TiO_2 and HNTs, respectively).

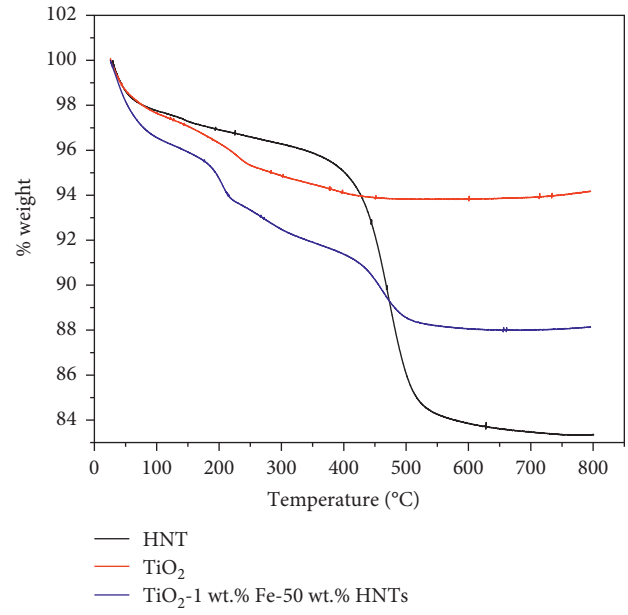

Figure 5: TGA curves for HNTs, TiO_2, and TiO_2-Fe-HNTs.

The scanning electron microscopy images of HNTs showed tubular structure with an uneven length and diameter of the tubes (Figure 7(a)). The morphology and structure of the HNTs did not change as observed in the SEM images of the composite (TiO_2-1 wt.% Fe-50 wt.% HNTs). However, agglomeration of the individual tubes can be seen in Figure 7(b). This is probably due to the growth of TiO_2-Fe crystals on the outer surface of the HNTs. It was observed at a relatively higher magnification (Figure 7(c)) that the TiO_2-Fe crystals settled on the outer surface of the HNTs. This is expected to enhance the aqueous dispersity of the composite as HNTs have been reported to possess high dispersity in water [30]. Enhanced aqueous dispersity will increase the proximity between water-soluble pollutants and the composite and result in improved photocatalysis and adsorption. The EDX analysis as shown in Figures 7(d) and 7(e) established that Al, Si, Fe, O, and Ti are present in the composite material. The atomic ratio of Al to Si is ca. 1. From the chemical formula of HNTs $(Al_2Si_2O_5(OH)_4 \cdot nH_2O)$, $n(Si)/n(Al)$ is 1. This was

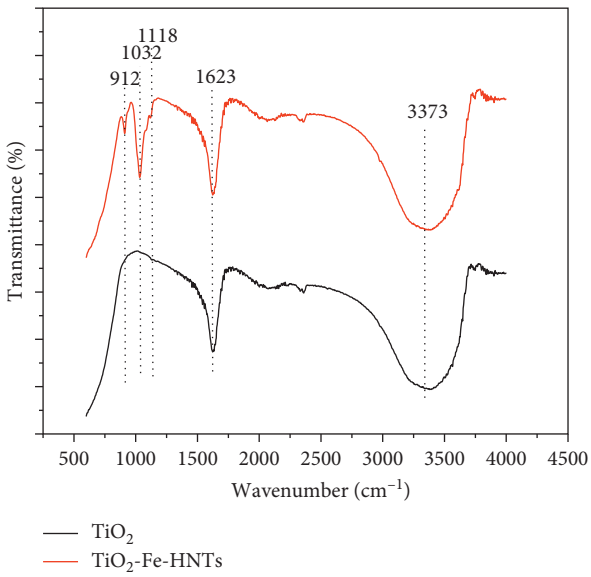

Figure 6: FTIR spectra of TiO_2 and TiO_2-Fe-HNTs.

confirmed from the table in Figure 7. In addition, the wt.% of Fe in the composite material used for this analysis was 1%. This was also confirmed by the EDX results which detected Fe (0.83 wt.%).

Since TiO_2 is a well-known photocatalyst, the effect of HNTs and Fe on the optical property of the TiO_2-Fe-HNT composite was examined using diffused reflectance spectroscopy (DRS), and the result is presented in Figure 8.

TiO_2 recorded ca. 100% reflectance in the visible region of the solar spectrum as can be seen in Figure 8. This implies that TiO_2 did not absorb visible light radiation. However, the reflectance by TiO_2 was almost zero in the ultraviolet region, implying that TiO_2 is active in the UV region of the electromagnetic spectrum. Addition of Fe and HNTs resulted in a decrease in the reflectance in the visible light region and a slight increase in reflectance in the UV region, meaning that the composite was photoactive in both ultraviolet and visible regions of the solar spectrum. The percentage of light absorption in the visible region increased with increasing wt.% of Fe. The optical band gap (BG) was also estimated using the Kubelka–Munk method. The estimated BG was 3.31, 3.24, and 3.2 eV for TiO_2, TiO_2-1 wt.% Fe-50 wt.% HNTs, and TiO_2-2 wt.% Fe-50 wt.% HNTs, respectively. The Fe and halloysite nanotubes did not influence to a greater extent the optical band gap of the composite.

3.3. Adsorption and Photocatalysis of TiO_2 and TiO_2-Fe-HNT Composite. The potential usage of the synthesized nanocomposite in water purification was examined through adsorption and photocatalytic processes using model pollutants such as water-soluble dyes (rhodamine B and methylene blue), pharmaceutical drug waste (naproxen sodium), and pesticide (imidacloprid). The results for the adsorption and photocatalytic studies using methylene blue are presented in Figure 1. The first thirty minutes represent the adsorption of methylene blue by TiO_2 and TiO_2-Fe-HNTs in the dark. The light was turned on after 30 minutes. The adsorption of methylene blue increased with increasing amount of HNTs used in the synthesis of the composite.

TiO_2 adsorbed ca. 4% of the methylene blue. Within the same period (30 minutes in the dark), TiO_2-1 wt.% Fe-25 wt.% HNTs, TiO_2-1 wt.% Fe-50 wt.% HNTs, and TiO_2-1 wt.% Fe-60 wt.% HNTs adsorbed 28, 50, and 60% of methylene blue, respectively. Methylene blue is positively charged when in solution. On the contrary, HNTs possess a negatively charged surface. The high adsorption recorded resulted from the electrostatic interaction between the cationic methylene blue and the anionic surface of HNTs. After the adsorption process, the composite-methylene blue solution was irradiated with tungsten halogen lamp to start the photocatalysis process. The photocatalytic efficiency of TiO_2-Fe-HNTs was observed to be lower than that of the pristine TiO_2. As revealed in the SEM images, the TiO_2 crystals were deposited onto the HNTs. Adsorption of the methylene blue dye by HNTs therefore enhanced the proximity between the pollutant and the TiO_2-Fe photocatalyst. This is expected to enhance the photocatalytic activity. However, excessive adsorption of methylene blue may block the active sites of TiO_2-Fe from light (solar energy) and hinder photocatalysis. The decrease in photocatalytic activity of the composite material is therefore attributed to the excessive adsorption of the cationic methylene blue by the anionic HNTs. The adsorbed methylene blue blocked the light from reaching the photoactive active sites of the TiO_2-Fe. It can also be seen in Figure 1 that the photocatalytic efficiency of the composite material was fairly comparable even with increasing amount of HNTs used in the synthesis. As can be seen in the summary presented in Figure 1(b), the removal of the methylene blue is attributed to the combined effect of photocatalysis and adsorption. The total removal % of methylene blue by the TiO_2-Fe-HNT composite was therefore higher than that by TiO_2. However, it must be mentioned that the amount of the dye degraded through photocatalysis (as can be seen in Figure 1(b)) was relatively smaller when compared to the amount adsorbed.

The photocatalytic and adsorption potential of the composite material was again examined using rhodamine B dye. This study is necessary because the adsorption studies conducted revealed that rhodamine is not "excessively" adsorbed by HNTs. The photocatalytic effect of TiO_2-Fe-HNTs is expected to be more pronounced with rhodamine B than with methylene blue. The results are presented in Figure 2. TiO_2 adsorbed ca. 11% of the rhodamine B dye, while TiO_2-1 wt.% Fe-25 wt.% HNTs, TiO_2-1 wt.% Fe-50 wt.% HNTs, and TiO_2-1 wt.% Fe-60 wt.% HNTs adsorbed 20.7, 22.2, and 19.3%, respectively. Unlike methylene blue, the adsorption of rhodamine B by the composite was almost the same, irrespective of the amount of HNTs used in the synthesis of the composite. This suggests that the adsorption mechanism of methylene blue by the composite may be different from that of rhodamine B. The photodegradation efficiency of the composite material was higher than that of the pristine TiO_2. However, it can be seen in Figure 2(b) that, unlike methylene blue (Figure 1), for all the composite materials studied, removal of rhodamine

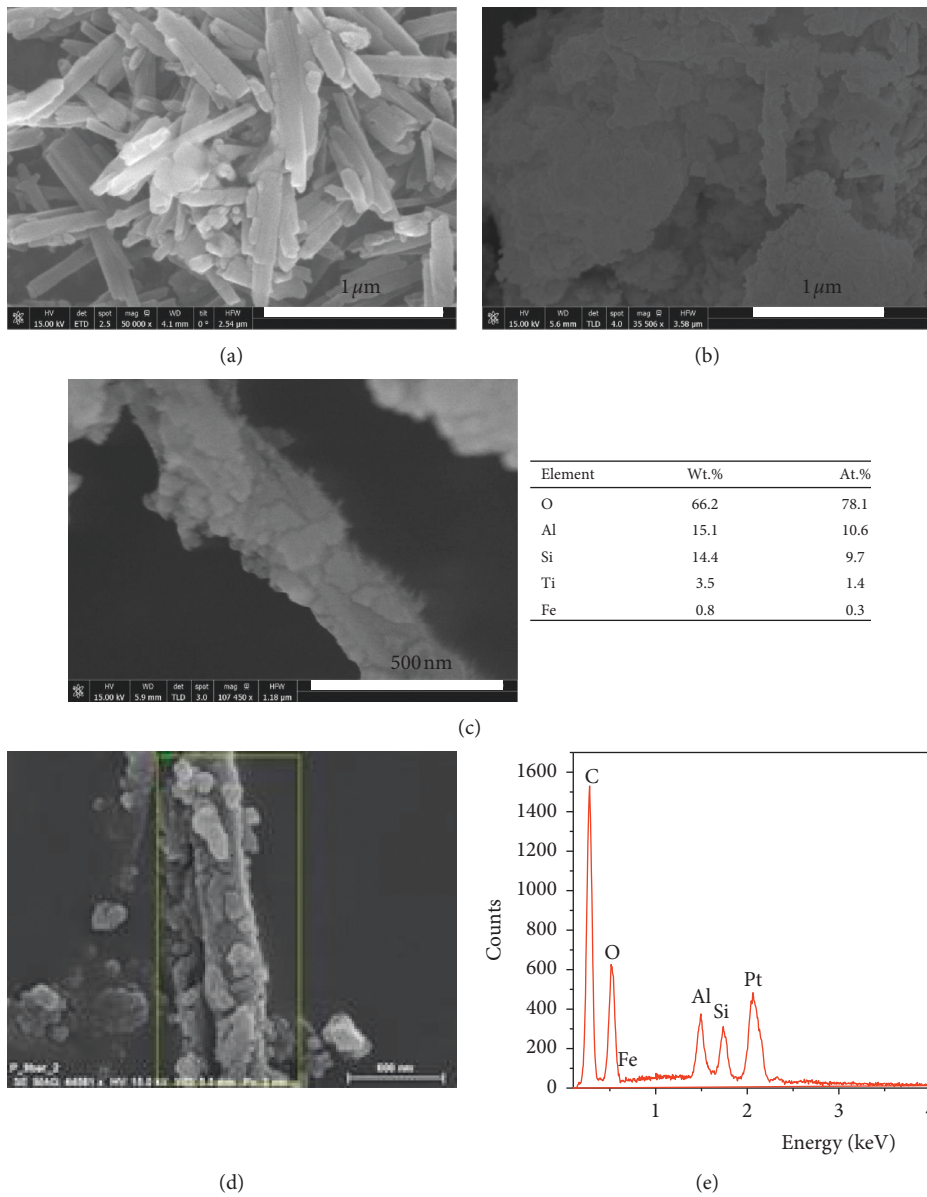

FIGURE 7: Scanning electron microscopy images of (a) HNTs, (b) TiO_2-1 wt.% Fe-50 wt.% HNTs at low magnification, (c) TiO_2-1 wt.% Fe-50 wt.% HNTs at high magnification. (d) The secondary reference image for the area EDX data was acquired (TiO_2-1 wt.% Fe-50 wt.% HNTs) and (e) EDX spectrum of TiO_2-1 wt.% Fe-50 wt.% HNTs.

B through photocatalysis was significantly higher than removal through adsorption. This reveals that though the removal of the pollutant is through photocatalysis and adsorption, the dominant process may be dependent on the nature of the pollutants and its interaction with the HNTs.

The pseudo-first-order rate constants for the photodegradation of methylene blue and rhodamine B dyes were calculated from equation (1), and the results are presented in Figure 3(a):

$$\ln \frac{C_t}{C_o} = kt. \quad (1)$$

Generally, for the degradation of rhodamine B, the rate constants of the TiO_2-Fe-HNT composites were significantly higher than that of TiO_2. However, for the degradation of methylene blue, the rate constant increased in the order T-1Fe-25 H < T < T-1Fe-50 H < T-1Fe-60 H. It was also observed that the rate constants for the photodegradation by the composite were higher for rhodamine B than methylene blue. The TiO_2 crystals were deposited onto the HNTs. The pronounced adsorption of methylene blue by the composite material resulted in the complete coverage of TiO_2. This might have reduced the absorption of photons by TiO_2 resulting in decreased photocatalytic activity and the smaller rate constant values obtained. Clay materials including HNTs have been reported to be poor adsorbents of rhodamine B dyes. This has been ascribed to the molecular size of rhodamine B and the nature of the interaction between rhodamine dyes and clays [40]. The lower adsorption of

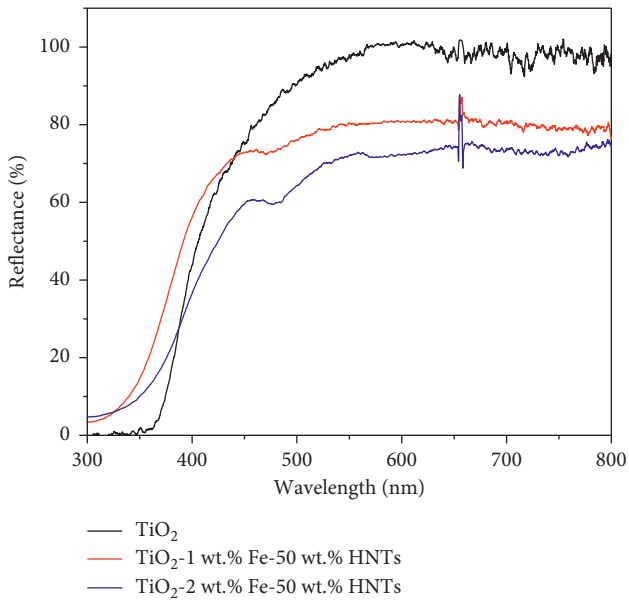

FIGURE 8: DRS analysis of TiO_2 and TiO_2-Fe-HNT composite.

rhodamine B ensured that the TiO_2 surface was not completely covered by the pollutants, and this allowed for enhanced absorption of photons. This enhanced the photocatalytic activity towards rhodamine B, and hence, the relatively higher rate constant values were observed. Therefore, to develop an efficient photocatalytic-adsorption process, a system must be designed in such a way that the amount of pollutants adsorbed does not exceed a threshold that may render the photocatalyst inactive.

The potential application of the synthesized composite in adsorbing and degrading other pollutants was examined using naproxen sodium (pharmaceutical drug) and imidacloprid (pesticides). The composite-pollutant solution mixture was stirred in the dark for 24 hours. The mixture was then irradiated with light, and the photodegradation was examined over specified time intervals. The UV-Vis absorption spectrum of these pollutants after adsorption and UV-Vis light irradiation are presented in Figure 9. The Fe-TiO_2-HNT composite adsorbed approximately 29.5% and 23.9% of the naproxen sodium and imidacloprid (Figure 9 and Table 1). The photocatalytic degradation of the naproxen sodium was more rapid than that of imidacloprid with a recorded photocatalytic degradation of 35.9% in 4 hours. The overall removal (adsorption and photocatalysis) efficiency was 65.4 and 41% for naproxen sodium and imidacloprid, respectively. The difference in the observed photocatalytic activity resulted from the differences in the structural stabilities of imidacloprid and naproxen sodium. Naproxen sodium is negatively charged in solution. HNTs have been reported to possess a slightly negatively charged outer surface and a positively charged inner lumen (lumen is the empty cylindrical space in the HNTs) [41]. This may result in an electrostatic interaction between the naproxen sodium and HNTs. It is obvious from Figure 9 and Table 1 that Fe-TiO_2-HNTs have the potential to remove (by adsorption and photodegradation) pesticides and pharmaceutical drug wastes from water bodies. It is however noted that unlike methylene blue and rhodamine B, a relatively longer time would be required for the photodegradation. Again, this may be due to the differences in the interaction between the pollutants and the Fe-TiO_2-HNTs as well as the structural stabilities of the various pollutants.

The photocatalytic activity of Fe-TiO_2-HNT was better than that of TiO_2. This observation can be attributed to a number of reasons. Irradiation of Fe-TiO_2-HNT with a light source resulted in the generation of electron-hole pair. Having in mind that the doping of TiO_2 was done using $FeCl_3$, Fe^{3+} can act as electron and hole trapping sites [19]. The photogenerated electrons may reduce Fe^{3+} to Fe^{2+}, while the photogenerated holes may oxidize Fe^{3+} to Fe^{4+}. The loss of d5 electronic configuration that arose from the reduction of Fe^{3+} to Fe^{2+} made Fe^{2+} unstable. Fe^{2+} formed may further be oxidized by the photogenerated holes back to Fe^{3+}. As already stated, other researchers have reported that Fe^{3+} may act as both photogenerated electron and hole trapping sites [42]. As a result, Fe^{3+} may be oxidized to Fe^{4+} by the photogenerated holes. Fe^{4+} formed may be reduced back to Fe^{3+} and result in the formation of hydroxyl radicals that may enhance the photodegradation efficiency. The Ti^{3+}/Ti^{4+} energy level lies close to the Fe^{2+}/Fe^{3+} energy level. As a result, electrons trapped by Fe^{3+} can easily be transferred to Ti^{4+} at the surface of TiO^2. Fe^{3+} therefore serves as an efficient electron trapping site [43]. The trapping of electrons by Fe^{3+} may reduce the electron-hole recombination, and as a result, it may improve the photocatalytic activity. In addition, the presence of HNTs also enhanced the photocatalytic activity. The SEM images in Figure 7 revealed that the Fe-TiO_2 crystals grew on the surface of HNTs. An intimate contact therefore exists between Fe-TiO_2 and HNTs. The photogenerated electrons will therefore not accumulate in Fe-TiO_2 and will be transferred from Fe-TiO_2 to HNTs due to unique charge characteristics of HNTs (Figure 10). Due to the surface charge characteristics of HNTs, HNTs also serve as electron trapping sites which further reduced the electron-hole recombination [44, 45]. The lumen of HNTs is slightly positively charged within the pH range of 2–8; hence, the photogenerated electrons can be attracted to the positively charged lumen. More holes will therefore be available to be utilized in the photodegradation of the organic pollutants.

The reactive species (RS) responsible for the Fe-TiO_2-HNT photocatalytic degradation of methylene blue was examined using DMSO, benzoquinone, and ethylenediamine tera-acetic acid disodium (EDTA-2Na). DMSO can be used as ·OH scavenger, while EDTA-2Na and benzoquinone scavenge h^+ and $\cdot O_2^-$, respectively [46]. The photodegradation efficiency after the addition of DMSO, benzoquinone, and EDTA-2Na were ca. 60.45%, 69.27%, and 51.13%, respectively, when compared to 71.86% in which no scavenger was added. This suggests that the main RS responsible for the photocatalytic degradation of methylene blue by Fe-TiO_2-HNTs are ·OH and h^+. Since Fe^{3+} and HNTs serve as electron trapping sites, more h^+ will be available for the photo-oxidation of the water-soluble dye. The photodegradation process is further enhanced by the

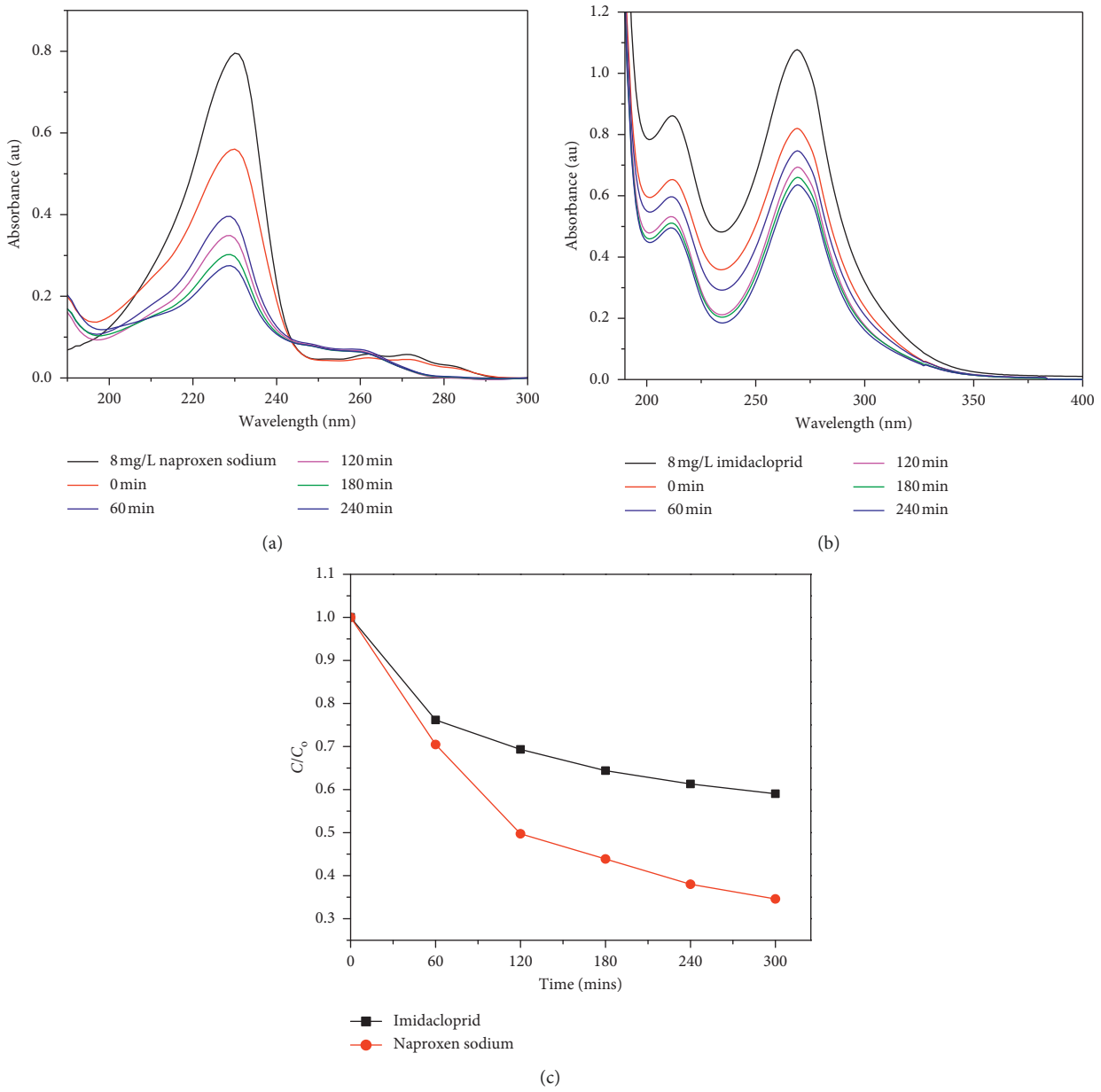

Figure 9: Adsorption and photodegradation of (a) naproxen sodium and (b) imidacloprid. (c) Comparing the adsorption and photodegradation of imidacloprid and naproxen sodium by the Fe-TiO_2-HNT composite.

Table 1: Summary of the adsorption and photodegradation efficiency.

Pollutant	Removal by adsorption (%)	Removal by photocatalysis (%)	Overall removal (%)	Photocatalysis rate constant (min^{-1})
Imidacloprid	23.9 ± 1.65	17.1 ± 1.87	41.0 ± 1.76	0.0012 ± 0.0001
Naproxen sodium	29.5 ± 0.91	35.9 ± 2.12	65.4 ± 1.52	0.0033 ± 0.0001

unique adsorption properties of HNTs. Since HNTs are good adsorbents for methylene blue and rhodamine B and the Fe-TiO_2 crystals grew on the surface of HNTs, the diffusion path of the pollutants to the surface active sites available for photocatalysis was reduced. This is expected to enhance the photodegradation efficiency.

3.4. Adsorption and Equilibrium Kinetics. The potential of the TiO_2-Fe-HNT composite to adsorb MB and RhB dye molecules from solution was examined using the kinetics and isotherm models. The pseudo-first-order (PFO) (equation (2)), pseudo-second-order (PSO) (equation (3)), and Intraparticle models (equation (4)) were used to

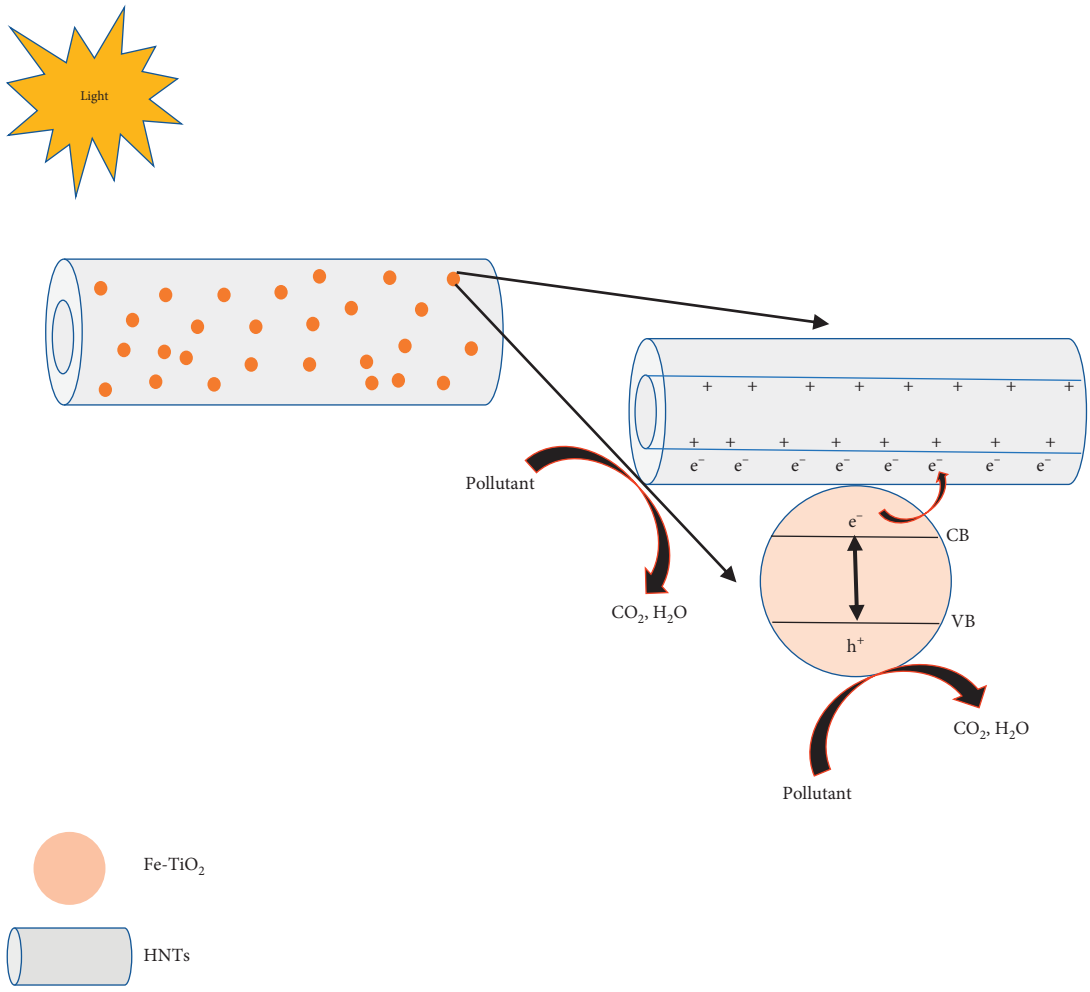

Figure 10: Schematic representation of the photocatalytic degradation of organic pollutants.

describe the adsorption kinetics of the MB and RhB dye molecules [41, 47–49]:

$$\log(q_e - q_t) = \log q_e - \frac{k_1}{2.303}t, \tag{2}$$

$$\frac{t}{q_t} = \frac{1}{k_2 q_e^2} + \frac{t}{q_e}, \tag{3}$$

$$q_t = k_i t^{0.5} + C_i, \tag{4}$$

where q_t (mg/g) represents the quantity of dye adsorbed at time "t" in minutes, q_e represent the equilibrium dye adsorption capacity (mg/g), k_1, k_2, and k_i represent the rate constant of PFO, PSO, and intraparticle models, respectively.

The adsorption data were fitted unto these models with the best-fit model were selected based on the highest, R^2, values as shown in Figures 11(a) and 11(b). From the study, the adsorption mechanisms were controlled by the PSO model with the highest R^2 values of 0.9961 and 0.9993 as compared to the PFO model with R^2 values of 0.9875 and 0.9589 for MB and RhB, respectively. The PSO model adsorption indicates that the adsorption of both MB and RhB molecules were controlled by chemisorption as a result of chemical bonds obtained through the exchange of electrons between the TiO_2-Fe-HNTs and cationic dye molecules [50].

Moreover, the rate-controlling steps of the adsorption process were further described using the intraparticle model as shown in Figure 11(c). Overall, the graph depicts a two-phase total adsorption process of the dye molecules, showing a rapid instantaneous adsorption within the first 30 minutes followed by a gradual second phase which attains saturation. The excellent adsorption process was enhanced by the aqueous dispersity of the composite provided by the TiO_2-Fe crystals on the outer surface of the tubular structured HNTs as seen in Figure 7. Also the surface of the TiO_2 is enriched with hydroxyl group which provides a negatively charged surface for efficient adsorption of cationic dyes [51]. In addition, the cylindrical hollow-shaped halloysite made up of several packed aluminosilicate sheets causes the inner lumen to be positively charged due to its aluminum oxide bonds, while its outer surface carries negative charges due to its silica surface. This unique bivalent surface morphology makes halloysite an excellent adsorbent to attract negative charge pollutant into its lumen and positive charge pollutant onto its outer surface [28, 52]. The presence of numerous vacant adsorption sites and dye molecules caused the

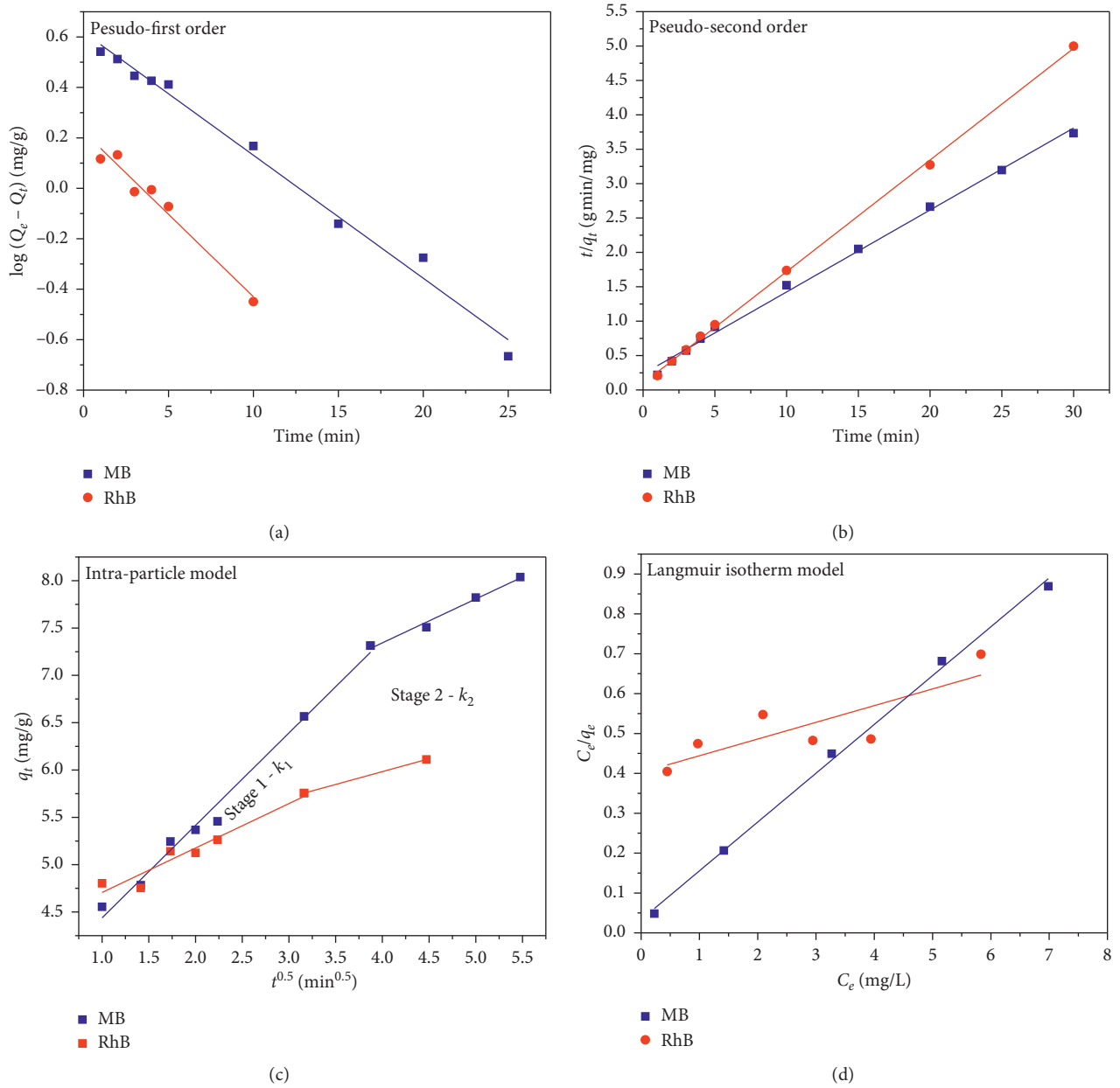

Figure 11: Continued.

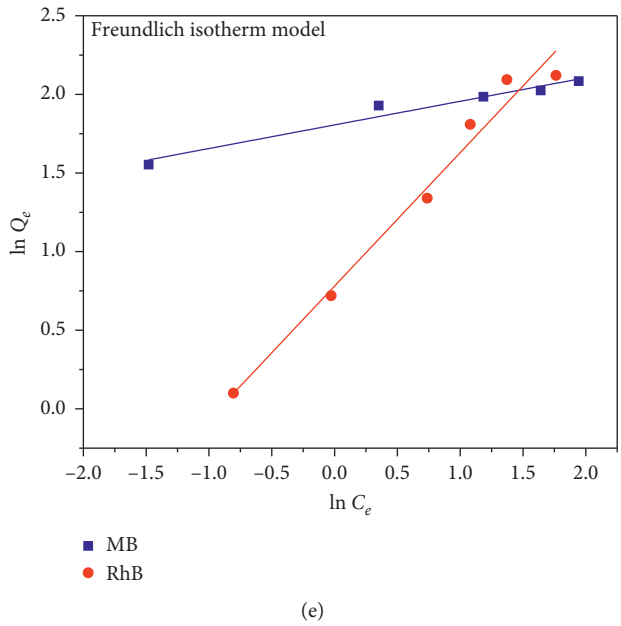

(e)

Figure 11: Kinetic and sorption models describing the adsorption process. (a) Pseudo-first order. (b) Pseudo-second order. (c) Intraparticle. (d) The Langmuir and (e) Freundlich models.

establishment of a higher concentration gradient between the water-soluble dyes and TiO_2-Fe-HNTs, resulting in an increase in the driving force and transfer of MB and RhB molecules from solution to readily bind with the vacant active sites present within the lumen and on the surface of the HNT. This resulted in higher instantaneous adsorption resulting from increased electrostatic attraction between the vacant adsorption sites and the dye molecules. This fast adsorption kinetics was observed in the first stage with steeper slopes during 30 minutes of adsorption. The first stage of the adsorption process obtained steeper slopes of 0.10233 and 0.14032 for MB and RhB, respectively. The adsorption of RhB attained a higher PSO rate constant as compared to MB. This indicates that the RhB molecules displayed a faster adsorption kinetic with a higher adsorption rate than MB molecules indicating that the structure of the halloysite and the nature of the molecules played a major role in the adsorption process. Though both MB and RhB are cationic dyes, MB dyes are regarded as purely cationic in nature due to the positive diethylamine group present in its molecules, while the zwitterionic nature of RhB molecules possesses both positive diethylamine and negative carboxylic group within its molecules [51]. The adsorption of MB molecules only occurred on the surface of the HNT, while the bivalent surface of the HNT allowed the adsorption of the positive diethylamine group onto the surface and the carboxylic group into the lumen of the HNT, making the RhB molecules to be preferentially adsorbed [28, 51, 52].

The second stage of the dye adsorption process represented a more gradual adsorption process with rate constants of 0.05229 and 0.02903 for MB and RhB, respectively, till equilibrium was reached. The gradual diffusion process indicates that there was a lower concentration gradient and more of the vacant active sites were occupied by dye molecules leaving few active sites on the outer surface and within the lumen of the HNTs for effective adsorption. The intraparticle model also indicates that the adsorption process was controlled by film, pore, or surface diffusion or a combination during the adsorption phenomenon on the pore surface [49]. The few vacant active sites were occupied by the dye molecule until all adsorption sites got occupied implying that there was virtually no further adsorption taking place at equilibrium.

Moreover, the Langmuir (equation (5)) and Freundlich (equation (6)) isotherm models were further used to analyze the interaction and adsorption capacity of the TiO_2-Fe-HNTs to adsorb MB and RhB dye molecules [53, 54]:

$$\frac{C_e}{q_e} = \frac{1}{Q_m K_L} + \frac{C_e}{Q_m}, \tag{5}$$

$$\ln Q_e = \ln K_F + \frac{1}{n_f} \ln C_e, \tag{6}$$

where Q_m (mg/g) represents the maximum adsorption capacity at monolayer coverage and K_F (mg/g) and K_L (L/mg) represent the Freundlich and Langmuir adsorption constant (mg/g), respectively. C_e (mg/L) and Q_e represent the concentration of the adsorbate and the adsorption capacity of the adsorbent at equilibrium, respectively. In addition, the heterogeneity factor, n, in the Freundlich model within the range of 1 to 10 confirms a favorable adsorption. A smaller value of $1/n$ (below unity) indicates a high adsorption intensity. Also, the separation factor, R_L (equation (7)) within the range value of $0 < R_L < 1$ indicates the favorability of the Langmuir isotherm model during the adsorption process:

$$R_L = \frac{1}{1 + K_L C_o}, \tag{7}$$

Table 2: Summary of data fitted onto various kinetic models.

Models	Methylene blue (MB)	Rhodamine B (RhB)
Pseudo-first-order kinetic model		
R^2	0.988	0.959
K_1 (min^{-1})	0.112	0.151
Q_e (mg/g)	4.158	1.675
Pseudo-second-order kinetic model		
R^2	0.996	0.9993
K_2 (g min/mg)	0.458	0.9523
Q_e (mg/g)	4.280	10.268
Intraparticle diffusion model		
K_1 ($min^{0.5}$ g·mg^{-1})	0.102	0.140
K_2 ($min^{0.5}$ g·mg^{-1})	0.052	0.029
Langmuir isotherm model		
R^2	0.997	0.430
Q_m (mg/g)	8.169	25.867
K_L	0.270	10.756
R_L	0.649–0.270	0.0092–0.444
Freundlich isotherm model		
R^2	0.949	0.976
K_F	6.085	2.184
n	6.661	1.179

where C_o (mg/L) represent the initial concentrations of adsorbate. The Langmuir equation fitted the adsorption of MB molecules with a higher R^2 value of 0.9969, while the Freundlich equation fitted the adsorption of RhB molecules with a higher R^2 value of 0.9757. The Langmuir isotherm model indicates that the adsorption sites were identical and energetically charged where each adsorption site was responsible for adsorbing one dye molecule. This provided a homogeneous monolayer coverage of MB molecules on the surface of the adsorbent [55]. In addition, Q_m of the TiO_2-Fe-HNTs was found to be 8.2 mg/g and 25.9 mg/g for MB and RhB, respectively. On the contrary, the Freundlich isotherm best fitted the RhB adsorption mechanism which assumes a nonuniform distribution and a heterogeneous multilayer adsorption coverage of the adsorbed RhB molecules as a result of the adsorption of positive diethylamine group onto the surface and the carboxylic group in the lumen of the HNT [54]. The separation factor R_L lied within the range $0 < R_L < 1$, and heterogeneity factor, n, obtained as 1.1786 shows a higher affinity binding and a successful and favorable adsorption of MB and RhB molecules by the adsorbent [53]. The summary of parameters obtained from the kinetics and equilibrium models is presented in Table 2.

4. Conclusions

The TiO_2-Fe-HNT photocatalyst-adsorbent nanocomposite was successfully synthesized by the hydrothermal method and was photoactive in both UV and visible regions of the electromagnetic spectrum. SEM images revealed that the TiO_2-Fe crystals were formed on the outer surface of the HNTs. The synthesized photocatalyst-adsorbent material recorded an enhanced rhodamine B, methylene blue, naproxen sodium, and imidacloprid removal (photocatalysis and adsorption) efficiency when compared to pristine TiO_2. This observation was ascribed to the enhanced aqueous dispersity, adsorption, and photoactivity of the nanocomposite. An adsorption equilibrium data fitted well with the pseudo-second order for both methylene blue and rhodamine blue dyes indicating that the adsorption was controlled by chemisorption. The Langmuir and Freundlich isotherm models further described the adsorption interaction of methylene blue and rhodamine B molecules, respectively. This study shows potential application of the synthesized TiO_2-Fe-HNT nanocomposite in water treatment technologies.

Data Availability

The authors cannot share the data presented in this manuscript because they are part of an ongoing research work. The data would be made available when the entire research work is completed.

Conflicts of Interest

There are no conflicts of interest.

Acknowledgments

This work was financially supported through Commonwealth Academic Fellowship funded by the UK Government, the Alborada Trust Fund, and the CAPREx Fellowship.

References

[1] WHO/UNICEF, *2.1 Billion People Lack Safe Drinking Water at Home, More than Twice as Many Lack Safe Sanitation*, WHO/UNICEF, Geneva, Switzerland, 2017, https://www.unicef.org/press-releases/21-billion-people-lack-safe-drinking-water-home-more-twice-many-lack-safe-sanitation.

[2] P. K. Holt, G. W. Barton, and C. A. Mitchell, "The future for electrocoagulation as a localised water treatment technology," *Chemosphere*, vol. 59, no. 3, pp. 355–367, 2005.

[3] S. Natarajan, H. C. Bajaj, and R. J. Tayade, "Recent advances based on the synergetic effect of adsorption for removal of dyes from waste water using photocatalytic process," *Journal of Environmental Sciences*, vol. 65, pp. 201–222, 2018.

[4] I. Sirés and E. Brillas, "Remediation of water pollution caused by pharmaceutical residues based on electrochemical separation and degradation technologies: a review," *Environment International*, vol. 40, pp. 212–229, 2012.

[5] R. Khanna and S. Gupta, "Agrochemicals as a potential cause of ground water pollution: a review," *IJCS*, vol. 6, no. 3, pp. 985–990, 2018.

[6] S. Rajeshkumar, Y. Liu, X. Zhang, B. Ravikumar, G. Bai, and X. Li, "Studies on seasonal pollution of heavy metals in water, sediment, fish and oyster from the Meiliang Bay of Taihu Lake in China," *Chemosphere*, vol. 191, pp. 626–638, 2018.

[7] X. Fuku, N. Thovhogi, and M. Maaza, "Photocatalytic effect of green synthesised CuO nanoparticles on selected

environmental pollutants and pathogens," in *Proceedings of the AIP Conference*, May 2018.

[8] C. A. Menzie, B. B. Potocki, and J. Santodonato, "Exposure to carcinogenic PAHs in the environment," *Environmental Science & Technology*, vol. 26, no. 7, pp. 1278–1284, 1992.

[9] WHO, *Drinking-Water*, WHO, Geneva, Switzerland, 2018, https://www.who.int/news-room/fact-sheets/detail/drinking-water.

[10] M. N. Chong, B. Jin, C. W. K. Chow, and C. Saint, "Recent developments in photocatalytic water treatment technology: a review," *Water Research*, vol. 44, no. 10, pp. 2997–3027, 2010.

[11] V. K. Gupta, I. Ali, T. A. Saleh, A. Nayak, and S. Agarwal, "Chemical treatment technologies for waste-water recycling-an overview," *RSC Advances*, vol. 2, no. 16, pp. 6380–6388, 2012.

[12] C. G. Joseph, G. Li Puma, A. Bono, and D. Krishnaiah, "Sonophotocatalysis in advanced oxidation process: a short review," *Ultrasonics Sonochemistry*, vol. 16, no. 5, pp. 583–589, 2009.

[13] H. Agbe, E. Nyankson, N. Raza et al., "Recent advances in photoinduced catalysis for water splitting and environmental applications," *Journal of Industrial and Engineering Chemistry*, vol. 72, pp. 31–49, 2019.

[14] Y. Bi, S. Ouyang, N. Umezawa, J. Cao, and J. Ye, "Facet effect of single-crystalline Ag_3PO_4 sub-microcrystals on photocatalytic properties," *Journal of the American Chemical Society*, vol. 133, no. 17, pp. 6490–6492, 2011.

[15] M. Coto, G. Divitini, A. Dey et al., "Tuning the properties of a black TiO_2-Ag visible light photocatalyst produced by a rapid one-pot chemical reduction," *Materials Today Chemistry*, vol. 4, pp. 142–149, 2017.

[16] C. B. Ong, L. Y. Ng, and A. W. Mohammad, "A review of ZnO nanoparticles as solar photocatalysts: synthesis, mechanisms and applications," *Renewable and Sustainable Energy Reviews*, vol. 81, pp. 536–551, 2018.

[17] X. Lang, X. Chen, and J. Zhao, "Heterogeneous visible light photocatalysis for selective organic transformations," *Chemical Society Reviews*, vol. 43, no. 1, pp. 473–486, 2014.

[18] D. Dodoo-Arhin, F. P. Buabeng, J. M. Mwabora et al., "The effect of titanium dioxide synthesis technique and its photocatalytic degradation of organic dye pollutants," *Heliyon*, vol. 4, no. 7, Article ID e00681, 2018.

[19] S. Sood, A. Umar, S. K. Mehta, and S. K. Kansal, "Highly effective Fe-doped TiO_2 nanoparticles photocatalysts for visible-light driven photocatalytic degradation of toxic organic compounds," *Journal of Colloid and Interface Science*, vol. 450, pp. 213–223, 2015.

[20] J. Zhu, J. Ren, Y. Huo, Z. Bian, and H. Li, "Nanocrystalline Fe/TiO_2 visible photocatalyst with a mesoporous structure prepared via a nonhydrolytic Sol–Gel route," *The Journal of Physical Chemistry C*, vol. 111, no. 51, pp. 18965–18969, 2007.

[21] W.-K. Jo and C.-H. Yang, "Granular-activated carbon adsorption followed by annular-type photocatalytic system for control of indoor aromatic compounds," *Separation and Purification Technology*, vol. 66, no. 3, pp. 438–442, 2009.

[22] Z. Sun, X. He, J. Du, and W. Gong, "Synergistic effect of photocatalysis and adsorption of nano-TiO_2 self-assembled onto sulfanyl/activated carbon composite," *Environmental Science and Pollution Research*, vol. 23, no. 21, pp. 21733–21740, 2016.

[23] S. Fukahori, H. Ichiura, T. Kitaoka, and H. Tanaka, "Photocatalytic decomposition of bisphenol A in water using composite TiO_2-zeolite sheets prepared by a papermaking technique," *Environmental Science & Technology*, vol. 37, no. 5, pp. 1048–1051, 2003.

[24] Y. Zhang, Z.-R. Tang, X. Fu, and Y.-J. Xu, "TiO_2-graphene nanocomposites for gas-phase photocatalytic degradation of volatile aromatic pollutant: is TiO_2-graphene truly different from other TiO_2-carbon composite materials?," *ACS Nano*, vol. 4, no. 12, pp. 7303–7314, 2010.

[25] X. Fu, L. A. Clark, Q. Yang, and M. A. Anderson, "Enhanced photocatalytic performance of titania-based binary metal oxides: TiO_2/SiO_0 and TiO_2/ZrO_2," *Environmental Science & Technology*, vol. 30, no. 2, pp. 647–653, 1996.

[26] C. Anderson and A. J. Bard, "Improved photocatalytic activity and characterization of mixed TiO_2/SiO_2 and TiO_2/Al_2O_3 materials," *The Journal of Physical Chemistry B*, vol. 101, no. 14, pp. 2611–2616, 1997.

[27] K. Woan, G. Pyrgiotakis, and W. Sigmund, "Photocatalytic carbon-nanotube-TiO_2 composites," *Advanced Materials*, vol. 21, no. 21, pp. 2233–2239, 2009.

[28] P. Luo, Y. Zhao, B. Zhang, J. Liu, Y. Yang, and J. Liu, "Study on the adsorption of neutral red from aqueous solution onto halloysite nanotubes," *Water Research*, vol. 44, no. 5, pp. 1489–1497, 2010.

[29] K. Shankar, K. C. Tep, G. K. Mor, and C. A. Grimes, "An electrochemical strategy to incorporate nitrogen in nanostructured TiO_2 thin films: modification of bandgap and photoelectrochemical properties," *Journal of Physics D: Applied Physics*, vol. 39, no. 11, pp. 2361–2366, 2006.

[30] Y. M. Lvov, D. G. Shchukin, H. Möhwald, and R. R. Price, "Halloysite clay nanotubes for controlled release of protective agents," *ACS Nano*, vol. 2, no. 5, pp. 814–820, 2008.

[31] C. J. Ward, M. DeWitt, and E. W. Davis, "Halloysite nanoclay for controlled release applications," *ACS Symposium Series*, vol. 10, pp. 209–238, 2012.

[32] E. Nyankson, O. Olasehinde, V. T. John, and R. B. Gupta, "Surfactant-loaded halloysite clay nanotube dispersants for crude oil spill remediation," *Industrial & Engineering Chemistry Research*, vol. 54, no. 38, pp. 9328–9341, 2015.

[33] E. G. Bediako, E. Nyankson, D. Dodoo-Arhin et al., "Modified halloysite nanoclay as a vehicle for sustained drug delivery," *Heliyon*, vol. 4, no. 7, Article ID e00689, 2018.

[34] P. Huo, X. Gao, Z. Lu et al., "Photocatalytic degradation of antibiotics in water using metal ion@ TiO_2/HNTs under visible light," *Desalination and Water Treatment*, vol. 52, no. 37–39, pp. 6985–6995, 2014.

[35] D. Papoulis, "Halloysite based nanocomposites and photocatalysis: a Review," *Applied Clay Science*, vol. 168, pp. 164–174, 2019.

[36] Z. Li, W. Shen, W. He, and X. Zu, "Effect of Fe-doped TiO_2 nanoparticle derived from modified hydrothermal process on the photocatalytic degradation performance on methylene blue," *Journal of Hazardous Materials*, vol. 155, no. 3, pp. 590–594, 2008.

[37] J. Gardy, A. Hassanpour, X. Lai, and M. H. Ahmed, "Synthesis of $Ti(SO_4)O$ solid acid nano-catalyst and its application for biodiesel production from used cooking oil," *Applied Catalysis A: General*, vol. 527, pp. 81–95, 2016.

[38] R. Beranek and H. Kisch, "Tuning the optical and photoelectrochemical properties of surface-modified TiO_2," *Photochemical and Photobiological Sciences*, vol. 7, no. 1, pp. 40–48, 2008.

[39] K. Thangavelu, R. Annamalai, and D. Arulnandhi, "Preparation and characterization of nanosized TiO_2 powder by sol-gel precipitation route," *International Journal of Emerging*

Technology and Advanced Engineering, vol. 3, no. 1, pp. 636–639, 2013.

[40] E. Nyankson, J. K. Efavi, A. Yaya et al., "Synthesis and characterisation of zeolite-A and Zn-exchanged zeolite-A based on natural aluminosilicates and their potential applications," *Cogent Engineering*, vol. 5, no. 1, Article ID 1440480, 2018.

[41] L. Lisuzzo, G. Cavallaro, G. Lazzara, S. Milioto, F. Parisi, and Y. Stetsyshyn, "Stability of halloysite, imogolite, and boron nitride nanotubes in solvent media," *Applied Sciences*, vol. 8, no. 7, p. 1068, 2018.

[42] W.-C. Hung, Y.-C. Chen, H. Chu, and T.-K. Tseng, "Synthesis and characterization of TiO_2 and Fe/TiO_2 nanoparticles and their performance for photocatalytic degradation of 1,2-dichloroethane," *Applied Surface Science*, vol. 255, no. 5, pp. 2205–2213, 2008.

[43] J. Zhu, W. Zheng, B. He, J. Zhang, and M. Anpo, "Characterization of Fe–TiO_2 photocatalysts synthesized by hydrothermal method and their photocatalytic reactivity for photodegradation of XRG dye diluted in water," *Journal of Molecular Catalysis A: Chemical*, vol. 216, no. 1, pp. 35–43, 2004.

[44] L. You-ji and C. Wei, "Photocatalytic degradation of Rhodamine B using nanocrystalline TiO_2-zeolite surface composite catalysts: effects of photocatalytic condition on degradation efficiency," *Catalysis Science & Technology*, vol. 1, no. 5, pp. 802–809, 2011.

[45] E. Nyankson, B. Agyei-Tuffour, E. Annan et al., "Ag_2CO_3-halloysite nanotubes composite with enhanced removal efficiency for water soluble dyes," *Heliyon*, vol. 5, no. 6, Article ID e01969, 2019.

[46] A. Zhang, L. Zhang, H. Lu et al., "Facile synthesis of ternary Ag/AgBr-Ag_2CO_3 hybrids with enhanced photocatalytic removal of elemental mercury driven by visible light," *Journal of Hazardous Materials*, vol. 314, pp. 78–87, 2016.

[47] H. Qiu, L. Lv, B.-C. Pan, Q.-J. Zhang, W.-M. Zhang, and Q.-X. Zhang, "Critical review in adsorption kinetic models," *Journal of Zhejiang University-Science A*, vol. 10, no. 5, pp. 716–724, 2009.

[48] Y. S. Ho and G. McKay, "Pseudo-second order model for sorption processes," *Process Biochemistry*, vol. 34, no. 5, pp. 451–465, 1999.

[49] W. J. Weber and J. C. Morris, "Kinetics of adsorption on carbon from solution," *Journal of the Sanitary Engineering Division*, vol. 89, no. 2, pp. 31–60, 1963.

[50] E. Nyankson, J. Adjasoo, J. K. Efavi et al., "Characterization and evaluation of zeolite A/Fe_3O_4 nanocomposite as a potential adsorbent for removal of organic molecules from wastewater," *Journal of Chemistry*, vol. 2019, Article ID 8090756, 13 pages, 2019.

[51] I. S. Grover, S. Singh, and B. Pal, "The preparation, surface structure, zeta potential, surface charge density and photocatalytic activity of TiO_2 nanostructures of different shapes," *Applied Surface Science*, vol. 280, pp. 366–372, 2013.

[52] Y. Zhao, E. Abdullayev, A. Vasiliev, and Y. Lvov, "Halloysite nanotubule clay for efficient water purification," *Journal of Colloid and Interface Science*, vol. 406, pp. 121–129, 2013.

[53] I. Langmuir, "The adsorption of gases on plane surfaces of glass, mica and platinum," *Journal of the American Chemical Society*, vol. 40, no. 9, pp. 1361–1403, 1918.

[54] H. Freundlich, "Über die adsorption in lösungen," *Zeitschrift für physikalische Chemie*, vol. 57, no. 1, pp. 385–470, 1907.

[55] G. Moussavi, S. Talebi, M. Farrokhi, and R. M. Sabouti, "The investigation of mechanism, kinetic and isotherm of ammonia and humic acid co-adsorption onto natural zeolite," *Chemical Engineering Journal*, vol. 171, no. 3, pp. 1159–1169, 2011.